

Transverse Probing of Laser-Driven Plasma Wakefields Using Relativistic Electrons



Stony Brook
University

In partial fulfillment of the requirements for
the award of the degree of

Bachelor of Science
in Physics

Evan Trommer

2023

DEDICATION

To my parents and sister, for their endless support and belief in my capability to make an impact wherever I go.

ACKNOWLEDGEMENTS

This work was supported by the Undergraduate Research & Creative Activities (URECA) program at Stony Brook University. The authors would like to thank Stony Brook Research Computing and Cyberinfrastructure, and the Institute for Advanced Computational Science at Stony Brook University for access to the high-performance SeaWulf computing system, which was made possible by a \$1.4M National Science Foundation grant (#1531492).

I would like to thank my advisor, Professor Navid Vafaei-Najafabadi, for his support and invaluable advice as I joined the wakefield acceleration community, as well as providing me with a wealth of opportunities to grow as a scientist.

I would also like to thank Marisa Petrusky and Nicholas Manzella, whose previous work allowed me to conduct my research, for extensively walking me through their versions of the simulation code and answering my endless questions.

Finally, I would like to thank my closest friends, whose unwavering confidence in my abilities kept me motivated. My academic journey has been made all the more fulfilling with them by my side.

Abstract

Laser wakefield accelerators (LWFAs) have the capability to accelerate charged particles with a much greater force per distance traveled compared to typical radiofrequency cavity accelerators. Laser pulses sent through plasma form a bubble structure called a laser wakefield, the inside of which consists only of positive ions, and is surrounded by a thin layer of electrons. The resulting charge distribution forms high-gradient accelerating fields, as well as focusing fields in the transverse direction. While theoretical solutions for the electromagnetic focusing fields have been developed, and the high accelerating forces of these wakes have been demonstrated experimentally, the field structures have yet to be verified using experimental data. Verification and understanding of the electromagnetic field structure is crucial for being able to effectively utilize LWFA technology, as achieving high quality colliding beams gives physicists a higher probability of observing new phenomena. Our work simulates the transverse probing of laser wakefields using relativistic electrons. With these simulations, we study the behavior of the probing electrons through the implementation of filtering masks to investigate the focusing characteristics of electron “bands”. This allows us to study the electromagnetic forces by analyzing how the bands are deflected after interacting with the wakefield. This work culminates in the development of an analytic model to predict the point at which these bands reach a minimum width by using previous formulations of the focal length for a single electron. Hence, our simulation results potentially give a powerful experimental diagnostic for verifying the electromagnetic field structure, which provides an analytic framework needed for the first direct measurements of focusing forces in an LWFA at the Accelerator Test Facility at Brookhaven National Lab.

Contents

1	Introduction	2
1.1	Motivation	2
1.2	Background	3
1.3	Gap in Knowledge	3
1.4	The Laser-Wakefield Experiment at ATF	4
2	Methods	6
2.1	Coordinate System and Co-Moving Variable	7
2.1.1	The Quasi-static Approximation	10
2.2	Thin Lens Approximation	10
2.3	Spherical Wakefield Approximation	11
2.4	Simulation Tools	12
2.4.1	Creating Electron Bands	12
2.5	Analytical Focal Length Calculations	13
2.5.1	Focal Length with a Spherical Wakefield Model	16
2.5.2	Analytical Formula for the Minimum Width of Electron Bands	20
3	Results	22
3.1	Measurement of Minimum Widths for Thin Electron Bands	22
3.2	Curtain Masks	27
3.3	Exploration of the Focal Length for a Spherical Wakefield	29
4	Conclusion	32

Chapter 1

Introduction

1.1 Motivation

Particle accelerators have served to push the boundaries of the scientific community's understanding of the fundamental mechanisms that govern our universe, as well as driven advances in industrial processes, such as semiconductor chip manufacturing and radiation therapy [1]. Despite the numerous advances that radiofrequency (RF) cavity accelerators have contributed to, further research and applications require higher particle energies, which has typically been achieved by simply building larger accelerators. However, size and cost limitations for building higher energy accelerators using RF cavities are now being reached. A potential alternative that is more compact than conventional RF accelerators are linear laser wakefield accelerators (LWFAs).

While still in the early stages of development, LWFAs have already shown the potential to provide significantly greater accelerating forces than other particle accelerators. Recent experiments demonstrate the capability of LWFA's to create accelerating gradients as high as 39 GeV/m [2], while conventional RF cavity accelerators, such as the linear accelerator at SLAC National Accelerator Laboratory, typically only support gradients on the order of 10 – 100 MeV/m. A two to three order of magnitude increase in accelerating gradient would

allow for future accelerator facilities to be hundreds of meters in a straight line, instead of tens of kilometers in circumference, which could then help reduce the cost required to build and operate future accelerators. Thus, further study of LWFAs could have profound benefits for future physics research and other industrial applications.

1.2 Background

LWFAs operate by sending a high energy, ultrashort laser pulse through a quasi-neutral plasma to form plasma waves. The pulse exerts a ponderomotive force on electrons and kicks them out of the laser’s path, while leaving the much heavier ions behind. The electrons oscillate as they return to equilibrium and form a thin sheath around a spherical cavity of only positive ions. This structure is called the “blowout region” and it moves with the driving laser pulse near the speed of light. Electromagnetic (EM) accelerating and focusing fields are generated as a result of the charge distribution left in the wake. Then, electrons can be injected into the blowout region and accelerated to ultra-relativistic speeds. Additionally, the wake’s internal focusing fields provide the same function of focusing particle beams as quadrupole magnets in RF accelerators.

1.3 Gap in Knowledge

To understand the viability of LWFAs for future research applications, the emittance evolution of the accelerated electron beams inside the blowout region needs to be analyzed. Achieving and maintaining a low emittance particle beam is desirable for creating colliding beams with high brightness, which is an important factor for determining the merit of an accelerator. In LWFAs, theory predicts that the focusing forces inside the blowout region are linear. It is then presumed that these linear focusing forces will allow the accelerated beams to maintain a low emittance. However, the linearity of the focusing forces has yet to be experimentally demonstrated. Experimental measurements of the field structure will

allow us to test the linearity of the transverse forces and study the motion of electrons inside the wake, which will allow for more accurate characterizations of beam emittance evolution.

Measurements of the EM focusing fields will be done by probing low density plasma wakes ($n_e \sim 10^{17} \text{ cm}^{-3}$) with transverse electron probes. Conventionally, laser probes are used for characterizing the physical structures of wakefields in plasmas with densities higher than 10^{18} cm^{-3} by analyzing the accumulation of phase shifts. However, in low density plasmas with a comparatively low index of refraction, laser probes do not accumulate enough of a phase shift to make precise characterizations of EM fields. In contrast, electrons will directly interact with the transverse forces and be deflected as they move through the blowout region. The probe's density distribution after interacting with the wakefield can be imaged and used to reconstruct the wake's transverse and longitudinal electromagnetic fields [3]. This makes electron probes the most suitable tool for directly measuring the EM field structures. However, analytical frameworks for mapping electron behavior to the structure of the focusing fields is currently lacking. This thesis aims to contribute to the development of analytical tools that can be used to characterize the field structures from the resulting probe images.

1.4 The Laser-Wakefield Experiment at ATF

At the Accelerator Test Facility (ATF) at Brookhaven National Lab, LWFA experiments are conducted using a high-powered CO₂ laser. While petawatt-class laser pulses with wavelengths of about $\sim 1 \text{ } \mu\text{m}$ are typically required for driving plasma wakes, the CO₂ laser operates at a longer $9.2 \text{ } \mu\text{m}$ wavelength, which allows for lower laser powers of about 10 TW to be used while still efficiently driving the wakes. The ATF also has a linear accelerator (linac) that produces high quality, relativistic electron beams, and the linac is integrated at the interaction point with the plasma and CO₂ laser. The electrons can then be imaged after traversing the wakefield using beam profile monitors.

Much work has been done to model the ATF experiment using numerical simulation

software. This software allows us to study the behavior of electron beams affected by the wakefields, and thus explore methods in which we use electron probes to study the field structure in LWFA experiments before the experiments are actually performed. The research presented here will describe a new experimental diagnostic for measuring the transverse EM field structures in low-density plasma wakes using relativistic electron beams. A combination of analytic theory and simulation work is done in order to find such diagnostic methods.

Chapter 2 provides standard concepts in plasma physics and wakefield research, and explains how simulation software and analytical theories are used to develop methods for experimentally measuring the transverse EM field structure in plasma wakes. Chapter 3 shows the major results of the research performed. Finally, Chapter 4 is a summary of the work presented and applications of the results.

Chapter 2

Methods

In order to perform experimental measurements of the electromagnetic field structure inside plasma wakes, we need to have diagnostics for probing electron beams that give us information as to how their trajectories have been altered by the wakefield. To find such diagnostics, we use the Python software called QuEP (Quasi-static Electron Propagation) to simulate electron beam probes through LWFAs. QuEP uses particle-in-cell (PIC) simulations¹ of laser-driven wakefields and implements the ability to send electrons through the wakefield [4]. A recent undergraduate student updated the code to include the use of absorptive masks in front of the wakefield [5]. By studying the electrons' trajectories, with the application of a thin-lens model and absorptive masks, we will develop an experimental diagnostic for measuring the electromagnetic field structure inside plasma wakefields. In this section I will present the physics that leads to a diagnostic that is currently being used at experiments at the ATF. Additionally, an analytical model for the focusing of transverse-only electrons moving through a spherically shaped wakefield is developed.

¹Currently compatible with the relativistic Quasi-3D OSIRIS PIC simulations.

2.1 Coordinate System and Co-Moving Variable

This thesis will frequently make use of quantities for normalizing time and length scales. Time scales are normalized by the fundamental plasma frequency ω_p , which is given by

$$\omega_p^2 = \frac{n_e e^2}{m_e \epsilon_0} \quad (2.1)$$

where n_e is the number density of electrons, e is the electron charge, m_e is the electron mass, and ϵ_0 is the permittivity of free space [6]. Velocities are normalized in units of the speed of light in a vacuum $c = 1$, and momentum is normalized in units of $m_e c$. Lengths are expressed in units of c/ω_p , with ω_p^{-1} representing units of time. Finally, electromagnetic fields are normalized in units of $m_e c \omega_p / e$.

We use a Cartesian coordinate system in the QuEP code. As seen in Fig. 2.1, we send a laser pulse in the \hat{z} direction, which drives the plasma wakefield in the same direction. The laser is traveling near the speed of light c and for a time t . Next, we introduce a co-moving coordinate, $\xi = z - ct$, which allows us to follow the wakefields as they trail the laser pulse. In normalized units, this coordinate is expressed as $\xi = z - t$. An observing screen is then placed at some distance behind the wakefield in the \hat{x} direction to image probing electrons after they interact with the wake's electromagnetic fields.

Though the wakefield does not exhibit cylindrical symmetry, it does exhibit azimuthal symmetry around the z -axis; at each z coordinate, the wakefield has a circular shape in the $x - y$ plane. Therefore, it is sometimes convenient to use a cylindrical coordinate $r = \sqrt{x^2 + y^2}$ for the radial distance from the \hat{z} axis. We then define the quantity called the wakefield radius $r_b(\xi)$, which is a function of the co-moving variable. This quantity describes the distance from the \hat{z} axis to the edge of the blown out wake.

In our simulations, electrons are given initial coordinates (x_i, y_i, ξ_i) and momenta $(p_{x,i}, p_{y,i}, p_{z,i})$. These electrons are ultra-relativistic, with a Lorentz factor of $\gamma \geq 100$. For this work, we will primarily study the specific case of a probing electron with transverse-only

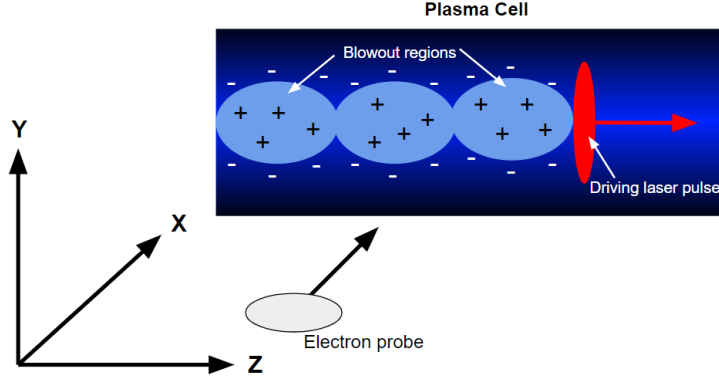


Figure 2.1: Visual representation of the coordinate system used in QuEP with an example of a plasma cell and electron probe. Picture repurposed from M. Petrusky *Picturing Plasma: Studying the Simulated Transverse Probing of Laser Wakefield Accelerators* [4].

momentum, so $(p_{x,i}, p_{y,i}, p_{z,i}) = (p, 0, 0)$. In a vacuum, such an electron will travel a distance $\Delta x = v_x \Delta t$, which we rearrange and write $\Delta t = \frac{\Delta x}{v_x}$ for the total time of the electron's propagation. The change in longitudinal position is then $\Delta z = v_z \Delta t = \frac{v_z}{v_x} \Delta x$. With the definition of the co-moving coordinate, the change in ξ is expressed by $\Delta \xi = \Delta z - \Delta t = \frac{v_z - 1}{v_x} \Delta x$. Since the electrons move only in the transverse direction with velocity $v_x \approx 1$, then $v_z = 0$, which gives us

$$\Delta \xi = -\Delta x \quad (2.2)$$

Thus, a transverse-only electron moves at a 45-degree angle in the $x - \xi$ plane. In differential form, Eq. 2.2 is re-written to be $d\xi = -dx$. Normally, we'd have to consider how the longitudinal forces may affect the electron's trajectory in ξ . However, our primary region of interest when probing the wakefields with electrons is where $dr_b/d\xi \approx 0$. The longitudinal electric fields in the wake are related to the wake radius by $E_z \propto dr_b/d\xi$ [7], so within the region of interest, these forces should have a negligible effect on the electrons' $\Delta \xi$ value.

To test that the longitudinal forces can be neglected, a simulation was performed with sending an electron with momentum (in normalized units) $(p_x, p_y, p_z) = (110, 0, 0)$ through a wakefield with electromagnetic fields shown in Fig. 3.1. The position was initialized such that when the electron reaches $(x, y, \xi) = (0, 0.25, -8.3)$, $r_b = r_{b,max}$ and so $dr_b/d\xi \approx 0$.

We then plot the change in the electron's momentum in each direction and we specifically compare the electron's p_y and p_z momentum after leaving the wakefield to p_x . We see from Fig. 2.2 that $\Delta p_x \approx 0.02$, $\Delta p_y \approx -0.15$ and $\Delta p_z \approx -0.02$. Since the total momentum is $|p| = \sqrt{p_x^2 + p_y^2 + p_z^2} \rightarrow \sqrt{(p_x + \Delta p_x)^2 + \Delta p_y^2 + \Delta p_z^2}$, and $\Delta p_y^2 + \Delta p_z^2 \ll (p_x + \Delta p_x)^2$, then the total momentum is approximately constant throughout the electron's transit of the wake. From Δp_z , we calculate $v_z \approx 2 \times 10^{-4}$ and then $d\xi = \frac{v_z - 1}{v_x} dx \approx -0.9998 dx$, so we have less than a 0.1% error in Eq. 2.2 in these simulations. This means that we can neglect the longitudinal force's impulse on the electron, and thus Eq. 2.2 is valid for a transverse electron passing through the blowout region where the top of the wake is flat.

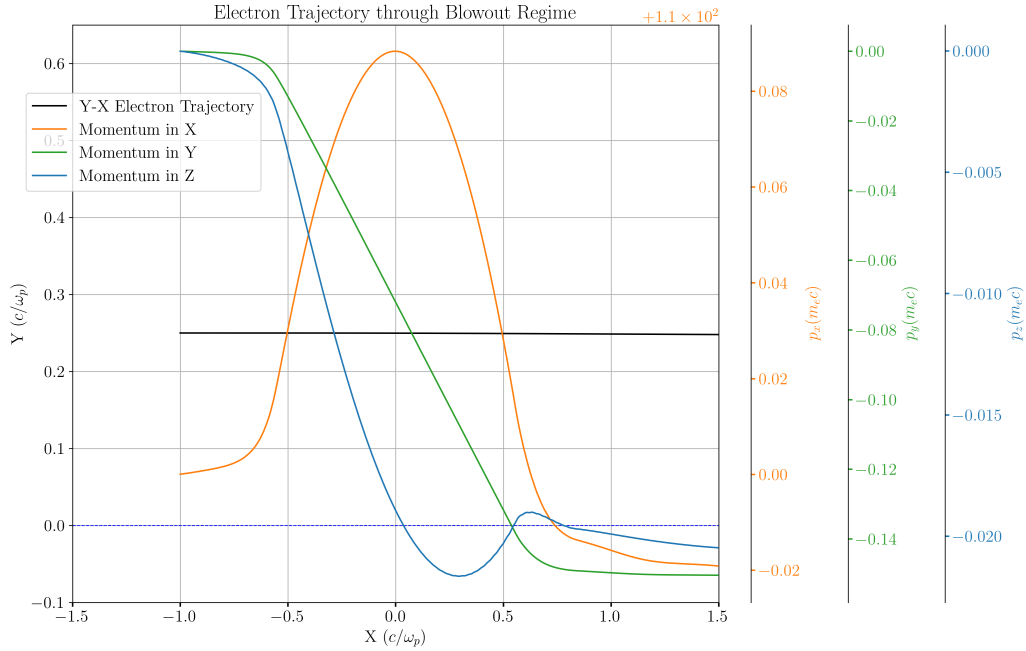


Figure 2.2: Plot of the electron's trajectory and momenta values in the $x - y$ plane while passing through the wakefield. The ballistic trajectory is plotted in black, p_x is plotted in orange, p_y is plotted in green, and p_z is plotted in blue. Note that the tick values for the x-momentum are actually $p_x - 110$.

2.1.1 The Quasi-static Approximation

The use of the co-moving variable ξ allows us to make the approximation that the laser-driven wakefield evolves very slowly over time during the time-scale of an electron probe's transit. This is called the quasi-static approximation, which is represented by the mathematical relation

$$\frac{\partial}{\partial z}, \frac{\partial^2}{\partial z^2} \ll \frac{\partial}{\partial \xi} \quad (2.3)$$

With such an approximation, the QuEP code can simply take a single frame of a wakefield from the OSIRIS PIC simulation, and propagate it through space and time at the group velocity of the laser pulse which, in this case, is $\vec{v}_g = c\hat{z}$. These PIC codes are computationally expensive, so using the approximation instead of using a self-consistent electromagnetic field map saves computation time for running these particle tracking simulations. We are therefore simulating electrons propagating through wakefields with a static electromagnetic field structure, meaning we only need to worry about the spatial variation of the wake's electromagnetic fields as electrons propagate through; there is no time variation in the fields that must be considered.

2.2 Thin Lens Approximation

In conventional optics, the thin lens approximation states that an incident light ray, parallel to the optical axis, will not change height while passing through the lens. However, the angle with respect to the optical axis of the exiting light ray will be different. This is represented by the equation

$$\begin{pmatrix} y \\ y' \end{pmatrix}_{exit} = \begin{pmatrix} 1 & 0 \\ -\frac{1}{f} & 1 \end{pmatrix} \begin{pmatrix} y \\ y' \end{pmatrix}_{incident} \quad (2.4)$$

where f is the focal length of the lens, and y and y' are the vertical position and angle of the light ray, respectively. Outside the lens, the light rays will follow a linear trajectory towards the optical axis.

Previous simulations have shown that an electron passing through the blowout regime of a wakefield at a height $|y_0| < r_b(\xi)$ will experience a negligible change in height, and then follow a linear ballistic trajectory outside of the plasma cell [4]. With this information, combined with the knowledge that the transverse forces in the blowout region of the wake are approximately linear, we model the plasma wakefield as a converging thin lens. Electrons moving parallel to the $x - \xi$ plane (i.e. $p_{y,i} = 0$) pass through a wakefield and get deflected to a focusing point (see Fig. 2.3). Analysis of the wakefield as a thin lens will allow us to directly study the forces inside the wake since, as will be discussed below, the focusing behavior of traversing electrons is directly related to the forces.

2.3 Spherical Wakefield Approximation

In the nonlinear regime, a plasma wakefield will not be spherically symmetric. However, there are certain conditions which will allow us to study a wakefield modeled as a sphere, and for that case we also want to understand the focusing behavior for such a wakefield shape. Nonlinear wakefield theory tells us that the equation of motion for a particle in the ultra-relativistic blowout regime of the wakefield (with a long ion channel) is given by [7]

$$r_b \frac{d^2 r_b}{d\xi^2} + 2 \left(\frac{dr_b}{d\xi} \right)^2 + 1 = 0 \quad (2.5)$$

Meanwhile, the equation for a circle is given by

$$r_b \frac{d^2 r_b}{d\xi^2} + \left(\frac{dr_b}{d\xi} \right)^2 + 1 = 0 \quad (2.6)$$

Notice that Eqs. 2.5 and 2.6 only differ by a factor of 2 in the $(dr_b/d\xi)^2$ term, which is a consequence of the wakefield typically having a steep gradient towards the back end of the blowout region for nonlinear wakes. When studying the motion of a particle near the center of the wakefield, where $dr_b/d\xi \rightarrow 0$, then Eqs. 2.5 and 2.6 are equal. This means that, in the center region of the blowout region where $r_b(\xi) = r_{b,max}$, $r_b(\xi)$ maps a circular wakefield. Since we are primarily concerned with studying electron trajectories after passing through the center of the wakefield, then we are motivated to model the wakefield as a sphere and understand how the focusing properties of probing electrons changes for this specific wakefield shape.

2.4 Simulation Tools

In accelerator physics, absorptive masks are used to create electron beams with certain transverse shapes. These masks were recently been implemented into the QuEP software library [5], and can either have a vertical or horizontal orientation, or both to create a grid. These masks are oriented in the $y - \xi$ plane, and the dimensions and placement of the mask mesh are initialized before the simulations are run. These masks are very powerful tools for simulations because we can limit our study to specific regions of the blowout regime, which, when combined with the focusing properties of probing electrons, will allow us to make characterizations of the electromagnetic forces in that part of the wake.

2.4.1 Creating Electron Bands

A particular shape for the electron beam that is useful for studying the focusing forces is a thin horizontal band. By sending bands through the wake, we can measure the intensity profiles at different distances, which gives us information about the focusing forces. To create this shape, we simulate two horizontal masks with vertical edges separated by some distance δy apart from one another. In order to study the focusing properties of these electrons, we

want these bands to have a width that is at least less than the radius of the wakefield – $\delta y < r_{b,max}$. As we will see in Sec. 2.5.2, it is actually desired that we make these bands as thin as physically possible since it will reduce the variation in focal lengths between electrons moving through the same wakefield radius.

2.5 Analytical Focal Length Calculations

Analytic wakefield theory tells us that the transverse electromagnetic forces in the blowout regime can be approximated to have a linear form

$$F_r = -k(\xi)r \quad (2.7)$$

where $k(\xi)$ is the “kicking strength” of the force. It follows that the force in the y –direction is [4]

$$F_y = -k(\xi)y_0 \quad (2.8)$$

with y_0 as the initial height of an electron. The linear focusing forces create an impulse on the traversing electron in the y –direction, thus deflecting the electrons towards the $x - \xi$ plane. In order to best study the focusing of electrons, we send them through the wakefield with initial y –momentum $p_{y,0} = 0$. Thus, the y –momentum an electron has after moving through the wakefield is given by the change in momentum Δp_y , which is

$$\begin{aligned} p_y &= \Delta p_y \\ &= \int F_y dt \\ &= -y_0 \int k(\xi) dt \\ &= -y_0 \int k(\xi) \frac{dt}{dx} dx \\ &= -y_0 \int k(x) \frac{dx}{v_x} \end{aligned}$$

$$p_y = -\frac{y_0}{v_x} \int k(x) dx$$

The angle θ towards the ξ -axis at which the electrons get deflected is given by

$$\tan \theta = \frac{p_y}{p_x}$$

Then, the focal length is found from the angle and the height of the electron outside the wake.

$$\begin{aligned} \Rightarrow f &= \frac{-y_0}{\tan \theta} \\ &= -y_0 \frac{p_x}{p_y} \\ f &= \frac{p_x v_x}{\int k(x) dx} \end{aligned} \tag{2.9}$$

While k is usually expressed as a function of position, in this work we take it to be constant, with a theoretical value of $k = 0.5$ in the blowout region [7]. So if $k(x) = k$ is constant, then Eq. 2.9 can be solved for in terms of the total distance travelled in x

$$f = \frac{p_x v_x}{k \Delta x} \tag{2.10}$$

Thus, if we can measure the total transverse distance an electron will travel in the blowout region, then we can calculate the focal length.

If we have an electron with both transverse and longitudinal momentum $\vec{p} = (p_x, 0, p_z)$ and send it through the wakefield where $dr_b/d\xi \approx 0$, as long as $v_z \approx c$, then $E_z \approx 0$ and thus the electron will observe a constant $r_b(\xi) = r_b$. Likewise, in this region the value of the field strength will be constant, and for simulations presented in this thesis, have a measured of $k \approx 0.475$ [4]. This situation is equivalent to modeling the wakefield as a cylinder. Then,

the total transverse distance traveled by an electron is

$$\Delta x = 2\sqrt{r_b^2 - y_0^2} \quad (2.11)$$

It follows that the focal length f of a single electron with an initial height y_0 is

$$\begin{aligned} f(y_0) &= \frac{p_x v_x}{2k\sqrt{r_b^2 - y_0^2}} \\ &= \frac{p_x v_x}{2kr_b} \left(1 - \left(\frac{y_0}{r_b}\right)^2\right)^{-1/2} \end{aligned} \quad (2.12)$$

Given Eq. 2.12 with $p_x \approx p$, $v_x \approx p/\gamma$, $F_{\perp, \max} = kr_b$, and $f_0 = p^2/2\gamma mkr_b$, then we arrive at

$$f(y_0) = \frac{p^2}{2\gamma mkr_b} \left(1 - \left(\frac{y_0}{r_b}\right)^2\right)^{-1/2} \quad (2.13)$$

$$= \frac{p^2}{2\gamma mF_{\perp, \max}} \left(1 - \left(\frac{y_0}{r_b}\right)^2\right)^{-1/2} \quad (2.14)$$

$$= f_0 \left(1 - \left(\frac{y_0}{r_b}\right)^2\right)^{-1/2} \quad (2.15)$$

For electrons sent at relatively small heights, the focal length is approximately a constant value f_0 . In our simulations with $\gamma = 110$, $k = 0.475$ and $r_b = 0.65 \text{ } c/\omega_p$, this constant is calculated to be $f_0 \approx 3 \text{ cm}$. The $(y_0/r_b)^2$ term in Eq. 2.13 is reminiscent of the “spherical aberration” effect in optics [4], and as electrons are sent closer to the edge of the wakefield, the expected focal length tends towards infinity. The appearance of the term $F_{\perp, \max} = kr_b$ is important; for electrons at small heights, we can arrange Eq. 2.14 to get

$$F_{\perp, \max} = \frac{p^2}{2\gamma m f_0} \quad (2.16)$$

In Eq. 2.16, p , m and γ are all known, and only f_0 needs to be experimentally measured in order to measure the transverse electromagnetic forces.

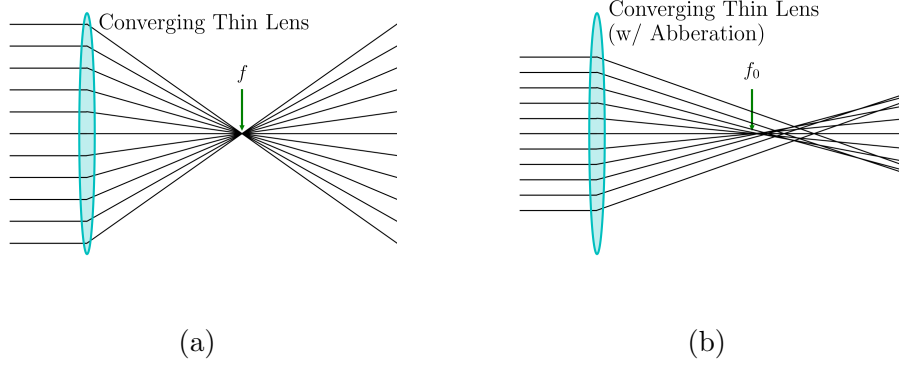


Figure 2.3: Illustration of the thin lens approximation. In (a) the blue ellipse represents a conventional thin glass lens, with the parallel lines representing rays of right. All the rays of light, independent of height, converge to a single point f . In (b) the blue ellipse represents a plasma wakefield with the parallel lines representing transverse electrons. The aberration of Eq. 2.13 is observable past the point f_0 along the horizontal axis.

2.5.1 Focal Length with a Spherical Wakefield Model

Now, we will study how Eq. 2.13 deviates if we have a spherical wakefield and using electron probes with only transverse momentum. Using our coordinate system, the equation that describes a spherical shell in 3D space is

$$x^2 + y^2 + \xi^2 = R_b^2 \quad (2.17)$$

where $R_b = r_{b,max}$. With this, the wakefield radius as a function of the longitudinal coordinate is

$$r_b(\xi_0)^2 + \xi_0^2 = R_b^2 \quad (2.18)$$

Here, ξ_0 is the point of intersection when the electron reaches $x = 0$. When $\xi_0 = \xi_c$, where ξ_c is the point at which $\left. \frac{dr_b}{d\xi} \right|_{\xi=\xi_c} = 0$, then $r_b(\xi_0) = R_b$ (see Fig. 2.4). Finally, for a transverse-only electron moving with speed $v_x \approx c$, since the wake also moves longitudinally with speed c , we use the relation in Eq. 2.2. For this case, an electron will move in a straight line, at a 45° angle, in the $x - \xi$ plane. For electrons at various heights y , we can model their trajectory as a diagonal plane, orthogonal to the $x - \xi$ plane. This intersecting plane is given

by the equation

$$(\xi - \xi_0) + x = 0 \quad (2.19)$$

To find the total time an electron spends in the wake, we need to find the total distance in x the electron travels within the wake. We can find the intersecting points of the plane and the spherical wake to find the entry and exit x -coordinates by plugging in Eq. 2.19 into 2.17:

$$x^2 + y^2 + (\xi_0 - x)^2 = R_b^2 \quad (2.20)$$

$$\Rightarrow 2x^2 + y^2 + \xi_0^2 - 2\xi_0 x = R_b^2 \quad (2.21)$$

$$\Rightarrow x^2 - \xi_0 x + \frac{1}{2} (y^2 + \xi_0^2 - R_b^2) = 0 \quad (2.22)$$

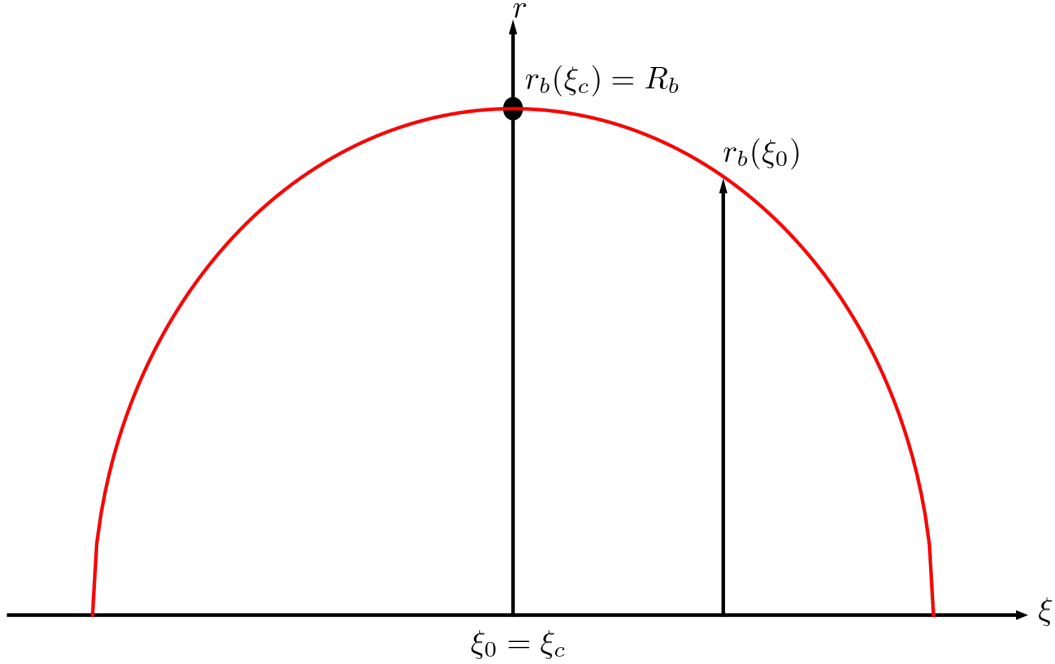


Figure 2.4: Visual representation of $r_b(\xi)$ for a spherical wakefield in the $r - \xi$ plane, with the longitudinal coordinate ξ as the horizontal axis and the radial position r as the vertical axis. The red semicircle represents the top half of the wakefield. At the point where $\xi_0 = \xi_c$, i.e. at the center of the wakefield, the wakefield radius has a maximum value. The arrow for $r_b(\xi_0)$ shows the wakefield radius when the electrons intersect the wake at some point different from the center, and it does not have the maximum value.

We then solve for x by simply using the quadratic formula:

$$x_{\pm} = \frac{\xi_0 \pm \sqrt{\xi_0^2 - 2(y^2 + \xi_0^2 - R_b^2)}}{2} \quad (2.23)$$

$$= \frac{\xi_0 \pm \sqrt{2R_b^2 - \xi_0^2 - 2y^2}}{2} \quad (2.24)$$

Using Eq. 2.18, the previous equation can be rewritten in terms of the variable radius.

$$x_{\pm} = \frac{\xi_0 \pm \sqrt{R_b^2 + r_b(\xi_0)^2 - 2y^2}}{2} \quad (2.25)$$

Then, we find the total x -distance by taking the difference of the exit and entry coordinates:

$$\begin{aligned} \Delta x &= x_+ - x_- \\ &= \left(\frac{\xi_0 + \sqrt{R_b^2 + r_b(\xi_0)^2 - 2y^2}}{2} \right) - \left(\frac{\xi_0 - \sqrt{R_b^2 + r_b(\xi_0)^2 - 2y^2}}{2} \right) \\ &= \sqrt{R_b^2 + r_b(\xi_0)^2 - 2y^2} \\ &\Rightarrow \Delta x = R_b \sqrt{1 + \left(\frac{r_b(\xi_0)}{R_b} \right)^2 - 2 \left(\frac{y}{R_b} \right)^2} \end{aligned} \quad (2.26)$$

Whereas Eq. 2.11 is only dependent on height since the wakefield radius is constant, Eq. 2.26 is also dependent on the ξ_0 position.

Now, we know the velocity of the electrons, and since it has been shown in simulations that $\Delta v_x \approx 0$, the total time of propagation is

$$\Delta t = \frac{\Delta x}{v_x} \quad (2.27)$$

$$= \frac{R_b}{v_x} \sqrt{1 + \left(\frac{r_b(\xi_0)}{R_b} \right)^2 - 2 \left(\frac{y}{R_b} \right)^2} \quad (2.28)$$

Since $dk(\xi)/d\xi \approx 0$ in the blowout region in our simulations, we can still approximate the transverse force as constant, which allows us to write the electron's momentum in y after

leaving the wakefield as

$$p_y = \Delta p_y \quad (2.29)$$

$$= \int F_y dt \quad (2.30)$$

$$\approx F_y \Delta t \quad (2.31)$$

$$= -k y_0 \Delta t \quad (2.32)$$

$$= -\frac{k y_0 R_b}{v_x} \sqrt{1 + \left(\frac{r_b(\xi_0)}{R_b}\right)^2 - 2 \left(\frac{y_0}{R_b}\right)^2} \quad (2.33)$$

The focal length is then given by

$$f = -\frac{p_x}{p_y} y_0 \quad (2.34)$$

$$= \frac{p_x v_x}{k y_0 R_b} y_0 \left(\sqrt{1 + \left(\frac{r_b(\xi_0)}{R_b}\right)^2 - 2 \left(\frac{y_0}{R_b}\right)^2} \right)^{-1} \quad (2.35)$$

$$f = \frac{p_x v_x}{k R_b} \left(1 + \left(\frac{r_b(\xi_0)}{R_b}\right)^2 - 2 \left(\frac{y_0}{R_b}\right)^2 \right)^{-1/2} \quad (2.36)$$

With a transverse-only electron, $p_x \approx p$, and $v_x \approx p/\gamma m$. Then we arrive at

$$f(y_0, \xi) = \frac{p^2}{\gamma m k R_b} \left(1 + \left(\frac{r_b(\xi_0)}{R_b}\right)^2 - 2 \left(\frac{y_0}{R_b}\right)^2 \right)^{-1/2} \quad (2.37)$$

So, we have derived an analytical expression for the focal length that is dependent on the intercepting coordinate ξ_0 . We can compare this to results from Eq. 2.13. Let's consider the particular case of sending an electron through the center of the wakefield, so $r_b(\xi_0) = R_b$, and at a small height $y_0/r_b(\xi_0) \ll 1$. Eq. 2.13 gives an expected focal length of $f = \frac{1}{2} \frac{p^2}{\gamma m k R_b}$, while Eq. 2.37 gives an expected focal length of $\frac{1}{\sqrt{2}} \frac{p^2}{\gamma m k R_b}$. The second result differs from previous expectations by a factor of $1/\sqrt{2}$, which is a surprisingly large difference in focal lengths, given the accuracy of Eq. 2.13 that has been previously shown within simulations

[4]. We will compare measurements of the distance travelled by an electron and focal length using Eqs. 2.26 and 2.37 to previous results in the following chapter.

2.5.2 Analytical Formula for the Minimum Width of Electron Bands

We know from Eq. 2.13 that electrons passing through the wakefield at different heights will have different focal lengths. Suppose we create a band of electrons with the vertical absorptive masks. Then the electrons at the bottom of the band will have a different focal length than electrons at the top of the band. By result of Eq. 2.13, how much the individual focal lengths differ between the bottom and top electrons is dependent on the width of the mask. Since the electrons all follow a linear trajectory outside of the wakefield, with the slopes depending on the focal lengths, then (ignoring electron-electron repulsion) we predict that their trajectories will intersect at some point similar to or beyond the focal length of electrons at the bottom of the band (see Fig. 2.3(b)). This intersection point is where the band has a minimum width.

To find the point of minimum width analytically, which we will denote as \tilde{f} , we start with a band of initial width δy such that electrons at the bottom of the band start at a height y_0 , and electrons at the top of the band have initial height $y_0 + \delta y$. After traveling through the wakefield, the electrons follow a linear, decreasing trajectory, represented by the equation $y = mx + b$, where the slope of the line is given by $m = -b/f(b)$. The two equations representing the trajectories are equal when the top and bottom of the band cross each other.

$$-\left(\frac{y_0}{f(y_0)}\right)x + y_0 = -\left(\frac{y_0 + \delta y}{f(y_0 + \delta y)}\right)x + y_0 + \delta y \quad (2.38)$$

$$\Rightarrow \left(\frac{y_0 + \delta y}{f(y_0 + \delta y)} - \frac{y_0}{f(y_0)}\right)x = \delta y \quad (2.39)$$

Rearranging to solve for where the band has a minimum width, i.e. at $x = \tilde{f}$, gives us

$$\tilde{f} = \delta y \left(\frac{y_0 + \delta y}{f(y_0 + \delta y)} - \frac{y_0}{f(y_0)} \right)^{-1} \quad (2.40)$$

$$= \delta y \left(\frac{(y_0 + \delta y)f(y_0) - y_0f(y_0 + \delta y)}{f(y_0)f(y_0 + \delta y)} \right)^{-1} \quad (2.41)$$

$$= \delta y \left(\frac{\delta y f(y_0) - y_0 [f(y_0 + \delta y) - f(y_0)]}{f(y_0)f(y_0 + \delta y)} \right)^{-1} \quad (2.42)$$

$$= \frac{\delta y f(y_0)f(y_0 + \delta y)}{\delta y f(y_0) - y_0 [f(y_0 + \delta y) - f(y_0)]} \quad (2.43)$$

$$= \frac{f(y_0)f(y_0 + \delta y)}{f(y_0) - y_0 \left[\frac{f(y_0 + \delta y) - f(y_0)}{\delta y} \right]} \quad (2.44)$$

Now, we consider the case of very thin bands, i.e. $\delta y \rightarrow 0$. This is motivated by the desire to have the electrons at the tops and bottoms of bands to have a relatively negligible difference in focal lengths at most heights, which implies the bands should always reach a minimum width at some distance behind the wake. Then, we can use the definition of the derivative to write

$$\begin{aligned} \lim_{\delta y \rightarrow 0} \tilde{f} &= \frac{f(y_0)f(y_0)}{f(y_0) - y_0 f'(y_0)} \\ &= \frac{f(y_0)}{1 - y_0 \frac{f'(y_0)}{f(y_0)}} \end{aligned} \quad (2.45)$$

Finally, when we take the limit of the thin bands sent near $y_0 = 0$, then using the binomial approximation gives

$$\tilde{f}(y_0, \delta y) \approx f(y_0) \left(1 + y_0 \frac{f'(y_0)}{f(y_0)} \right) \quad (2.46)$$

This is the point of minimum width of thin bands sent near the radial center of the wakefield. In theory, we can use masks to selectively send electrons through the center region of the wakefield and measure where this minimum width occurs. Then, we can use the focusing equations to calculate the transverse forces experienced by the electrons, and from there characterize the field structure inside the plasma wakes.

Chapter 3

Results

3.1 Measurement of Minimum Widths for Thin Electron Bands

Our simulations use electromagnetic field maps of laser-driven plasma wakefields generated by the Quasi-3D version of the OSIRIS particle-in-cell code [8]. The electric field map used for this study is shown in Fig. 3.1. In order to study the effects of just the wake's internal EM fields, we do not include the field of the laser pulse.

We note that in Fig. 3.1, the maximum wakefield radius $r_b(\xi) = R_b$ is measured at $\xi = -8.3$. We want to use Eq. 2.2 to align our electron beam probe such that when the beam reaches $x = 0$, the center of the beam will be under the center of the wakefield and experience the maximum transverse force $F_{\perp, max}$. Since the probing electrons are sent through in the $+\hat{x}$ direction, the probe was sent transversely through the wakefield with the center of the beam having initial position $(x_i, y_i, \xi_i) = (-1.0, 0.0, -7.3)$, and with transverse-only momentum $(p_x, p_y, p_z) = (110, 0, 0)$. The probe is modeled as a 2-D sheet of electrons, with a Gaussian density profile in the $y - \xi$ plane. Then, we used two vertical masks with edges separated by a distance $\delta y = 0.05 \text{ } c/\omega_p = 8.33 \text{ } \mu m$ to best test the approximation in Eq. 2.46. These bands span the length of the front and trailing bubbles in the blowout region,

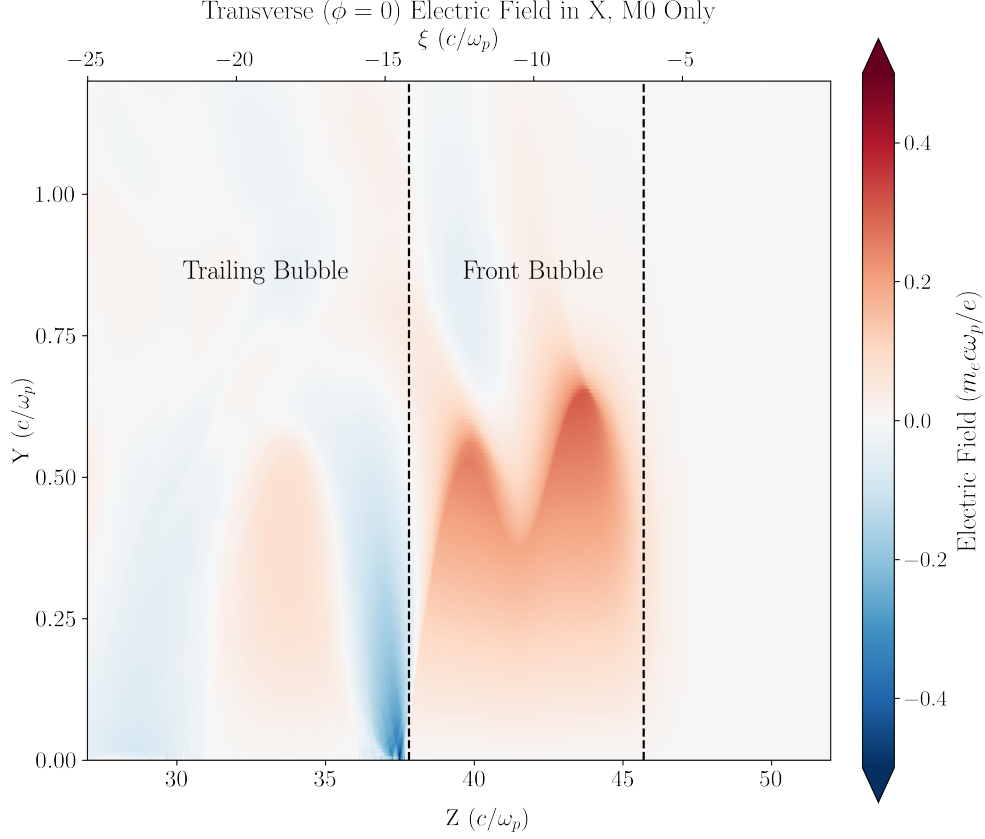


Figure 3.1: Transverse electric field map of the laser-driven wakefield with plasma density $n_e = 10^{15} \text{ cm}^{-3}$, with the laser's field excluded from the plot. The magnitude of the electric field is shown by the color axis on the right, with the longitudinal position and transverse height shown on the horizontal and vertical axes, respectively. The co-moving coordinate is also shown on the y -axis, at the top of the plot. The region marked between the black dashed lines from $z = 38$ to $z = 45.5$ is referred to as the front bubble of the blowout region.

labeled in Fig. 3.1. We also limited the bands' initial heights from $0.10 \leq y_0/r_b \leq 0.35$, since we are most interested in studying the focal length at small heights, where the focal length of an individual electron does not vary by more than 10% from f_0 .

For each band with height between $0.10 \leq y_0/r_b \leq 0.35$, we sent the band through the wakefield and created images of the band's density profile at distances between $0 \text{ mm} \leq x \leq 100 \text{ mm}$ behind the wakefield. The images were then compiled into an animation and we were able to observe by eye the evolution of the band's width. For each animation, we could record at what x value the band reached a minimum width and compare it to Eq. 2.46. We also recorded where the band crossed $y = 0$ as the band's focal length.

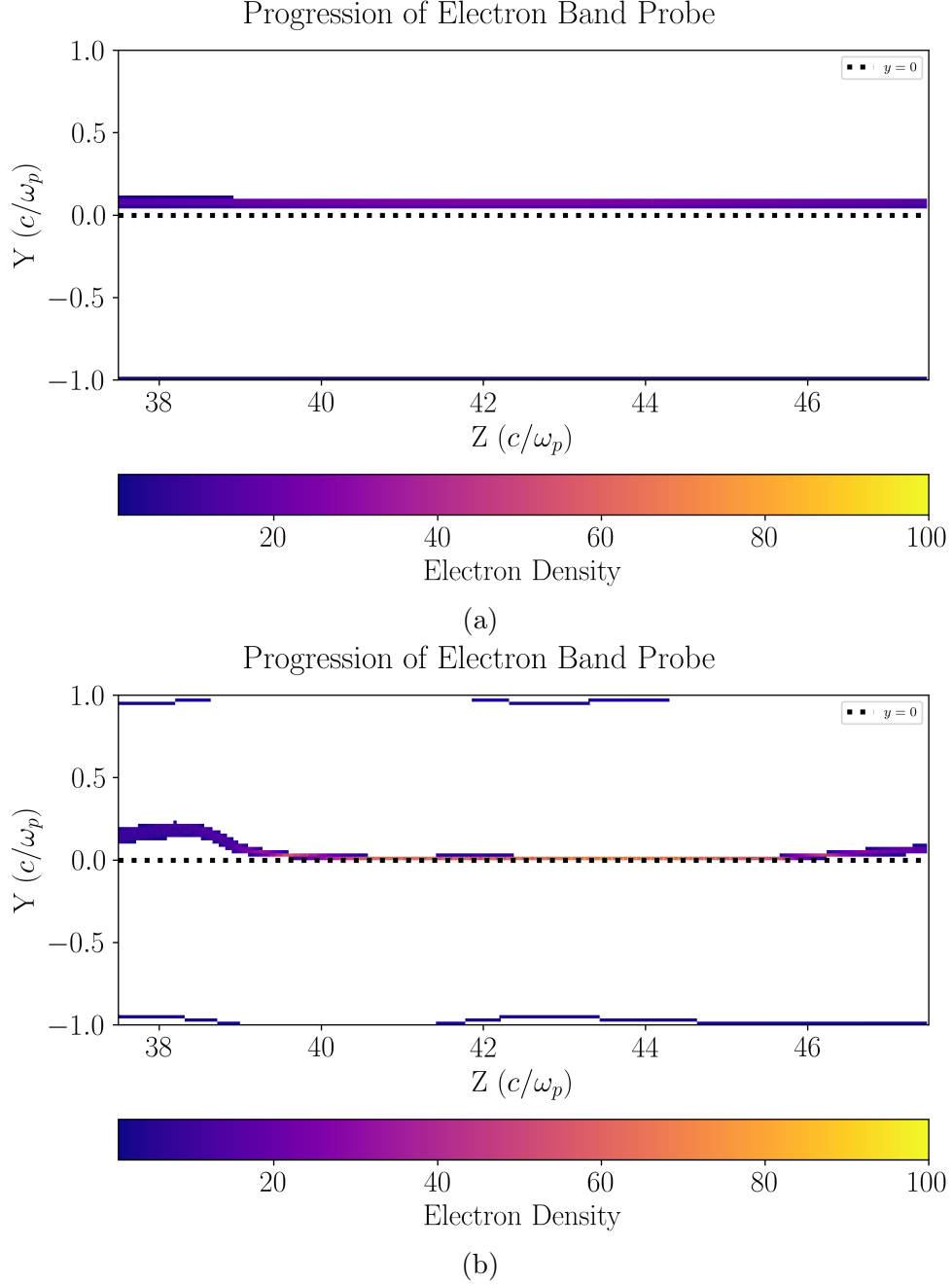


Figure 3.2: Simulations of an electron band of initial width $\delta y = 0.05 c/\omega_p$ at initial height $y_0/r_b = 0.1$. The horizontal axis is the longitudinal position of electrons in the beam, and the vertical axis is vertical position of electrons. The color axis shows electron density, with low densities represented with blue/purple colors and higher densities represented with orange/yellow colors. The black dotted line shows where $y = 0$. The imaging screen is set to be $x = 0$ mm behind the wakefield in Fig. 3.2(a), and $x = 28$ mm behind the wakefield in Fig. 3.2(b). In 3.2(b), we observed at this distance the band reaching it's minimal width as it crosses the y -axis.

In Fig. 3.2, we sent the band through the wakefield with initial height $y_0/r_b = 0.1$ and observed how the band changes in size, shape and position as we moved the observing plane from $x = 0$ mm, i.e. right behind the wakefield see (Fig. 3.2(a)), to $x = 28$ mm (see Fig. 3.2(b)). The width of the band does vary with z , but we focused on measuring the width at $z \approx 43.7$ since it is the position where the center of the beam is under the center of the front bubble. We measured that the band reaches it's minimum width at $x = 28$ mm. We also note that the focal length of the band occurs at the same distance. As seen in Eq. 2.46, for bands sent near the axis, the minimum width of the band occurs very near to where the band's focal length is, i.e. $\tilde{f}(y_0) \rightarrow f(y_0)$ as $y_0 \rightarrow 0$. However, the bands are expected to deviate from this behavior at higher heights due to the $f'(y_0)/f(y_0)$ term in Eq. 2.46, which goes as $y_0/(r_b(1 - (y_0/r_b)^2))$.

We observe in Fig. 3.3 that the data agrees well to the analytical approximation given by Eq. 2.46. Both the measured and expected distance at which the minimum widths occur increase with increasing height, and the increase becomes approximately quadratic at around $y_0/r_b = 0.25$. While the measured distance of minimum width is lower than expected at smaller heights, it still agrees within the estimated uncertainty to the expected values, though the uncertainty is large; the low precision is addressed in the next paragraph. The measured focal lengths have better agreement with the approximation at higher heights, though they are larger than predicted by the equation. We also observe that the band reaches it's minimum width at a distance different from when the band crosses the $y = 0$ line. While the red curve, which represents the focal length of the band, increases with increasing band height, it does not increase as much as the predicted distance at which the minimum width occurs. This is due to the fact that the band crossing the axis is representative of the focal length for a single electron at the top of the band; the focal length of the band does not account for it's width. This is expected from Eq. 2.46, as for non-small y_0/r_b , $\tilde{f}(y_0) > f(y_0)$, i.e. the x distance at which the minimum width occurs is generally further than the band's focal length. Overall, the approximation and the measured band focal lengths are consistent

Band Focal Length vs. Starting Height for $\delta y = 0.05$

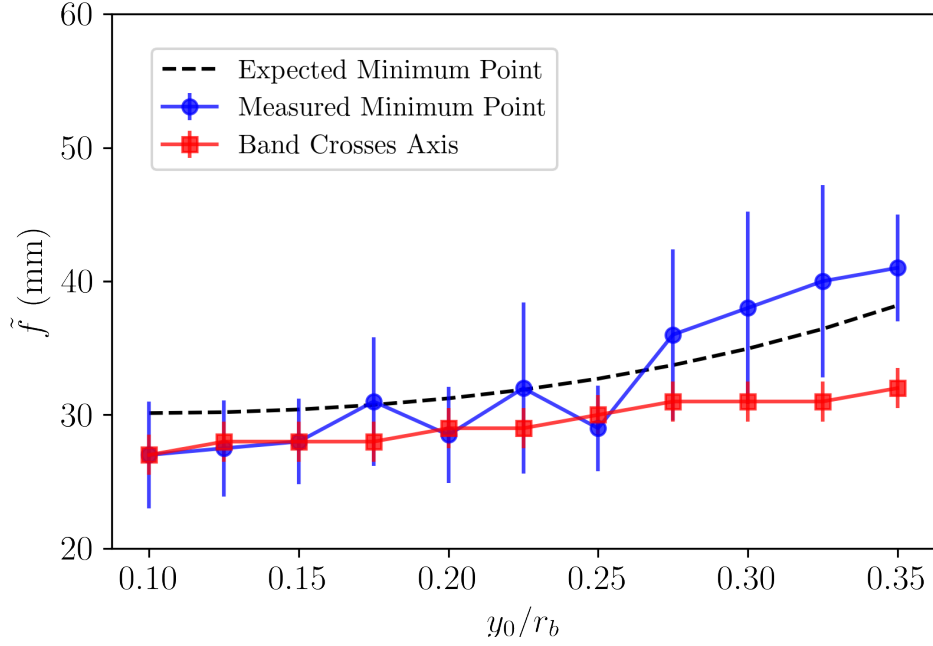


Figure 3.3: Plot showing the expected and measured minimum width positions of the bands. The horizontal axis is the height of the top of the band relative to the maximum wakefield radius $r_b = 0.65 c/\omega_p$, and the vertical axis represents the distance in x behind the wakefield that the band focusing is observed at. The black dashed line represents the expected results from the derived equation, and the blue dotted line is the measured focal length of the bands. The measured distance at which the band crosses $y = 0$ is shown in red. All curves are increasing as the relative height increases.

with one another.

The low precision is due to the data being taken using eye measurements with a low resolution. In the animations, the minimum width was never zero like we might have expected, so we had to make some estimation as to when the minimum width occurred. Thus, it is important that we address the magnitude of our errorbars. Though the bands generally behave as predicted by Eq. 2.46, the large errors still skew the interpretation of our results closer towards agreement. Further analysis with new numerical tools and simulations performed at higher resolutions are hence required to reduce the uncertainty in our measurements and to draw a more detailed conclusion about the analytical formula.

3.2 Curtain Masks

“Curtain” masks are a computational tool that were implemented into QuEP for the purpose of speeding up the analysis of many different masking configurations. The curtains are an optional step in the post-simulation process (see N. Manzella’s thesis [5] for an explanation of post-simulation processes) which dynamically changes the position of one of the mask’s edge. This can then be used to map the initial radial position of electrons to an observed feature in the electron profiles at the screen. The use of curtain masks is demonstrated in Figs. 3.4(a) and 3.4(b), where we have an unmasked probe and a probe that is vertically masked via a curtain, respectively. In Fig. 3.4(c), which is the result of propagating the unmasked electron probe in Fig. 3.4(a) through the wakefield, we see that there is a bright outlined region observed below $y = 0$, from $40 < z < 46$, representing a high density of electrons. Notably, the contour of this bright edge is similar to the outline of the wakefield radius in Fig. 3.1. We initially hypothesized that this outline may have been the result of electrons sent through the wakefield with height $y_0 = r_b(\xi)$; if true, then the curtains would provide us with a method of finding the maximum radius of the wakefield. The result of propagating the probe in Fig. 3.4(b) is shown in Fig. 3.4(d), and we observe that the edge of the mask had to be brought down to $y = 0.3$ to cause the bright outline to disappear.

The formation of the bright outline is important to study because it gives us insight into the focusing behavior of probing electrons. Notably, the edge of the curtain had to be brought down below the maximum radius of the wakefield before the outline disappeared, which contradicts our original hypothesis. What we now hypothesize is that the sharp feature is formed by electrons sent through the wakefield that have similar focal lengths. This is satisfied, as a result of Eq. 2.13, for electrons with heights between $0 < y/r_b < 0.5$, or electrons with heights below $y \approx 0.33$. By bringing the edge of the masks down to this height, we are effectively removing the effect of spherical aberration in Eq. 2.13 from our study. Then, at different screen distances we can make sets images like Fig. 3.4(c) and

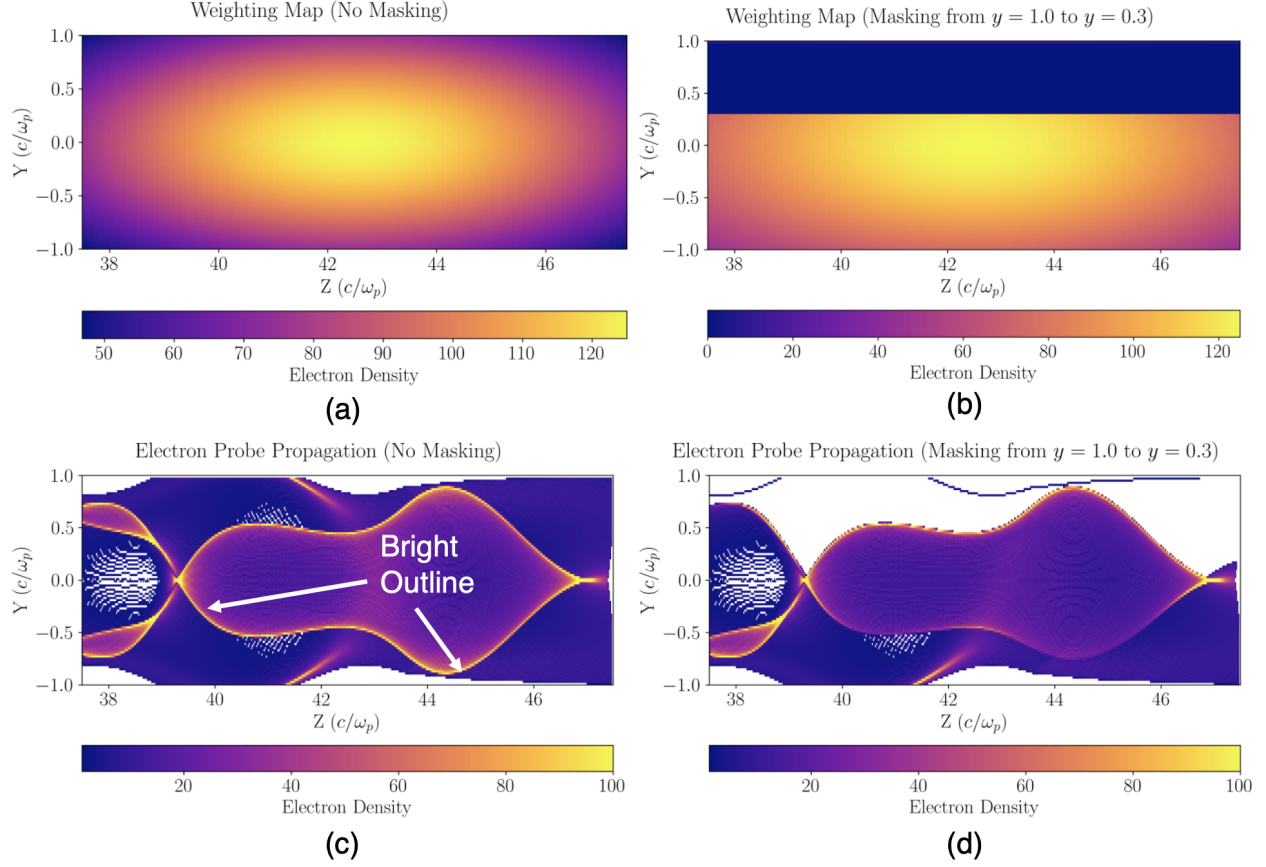


Figure 3.4: Plots showing an (a) unmasked and (b) masked electron probe, and the corresponding results after the probe is sent through the wakefield ((c) and (d), respectively). The horizontal axis is the longitudinal position of electrons in the beam, and the vertical axis is vertical position of electrons. The color axis shows electron density, with low densities represented with blue/purple colors and higher densities represented with orange/yellow colors. The imaging screen is chosen to be 11cm behind the wakefield. The curtain mask in (b) results in the bright outlined region, labeled in (c), being removed from the result.

(d) to test if this bright outline disappears whenever we bring the mask down to $y = 0.30$. Hence, we can use these curtain masks as a numerical diagnostic for qualitatively studying the focusing fields in different parts of the wake by understanding how bright features are formed by focusing electrons.

3.3 Exploration of the Focal Length for a Spherical Wakefield

We measured “experimental” focal lengths of electrons in simulations and compared the results to Eq. 2.37, which gives the expected focal lengths using a spherically-modeled wakefield. We also compare the measurements to Eq. 2.13, which is equivalent to comparing to the expected focal lengths of a cylindrically-modeled wakefield. Electrons are given transverse-only momentum in x , with $(p_x, p_y, p_z) = (110, 0, 0)$. They also have initial coordinates $(x_i, \xi_i) = (-1, -7.3)$ with heights ranging from $0 < y_0 < R_b$, such that the electron will see the maximum wakefield radius $r_b(\xi) = R_b$ at $x = 0$. Also, we are taking $R_b = 0.65 c/\omega_p$ and $k = 0.475$ in both Eqs. 2.13 and 2.37.

Intuitively, we would have expected Eq. 2.37 to converge to Eq. 2.13 for the case of $r_b(\xi_0) = R_b$. However, the measured focal lengths very closely match the cylindrical model up until $y_0/r_b \approx 0.7$, while the spherical model disagrees with the data at all the heights tested. The measured focal lengths increase with height, and the increase is approximately linear up until about $y_0/r_b \approx 0.8$. The expected focal lengths using both models increase with increasing height, and increase drastically past $y_0/r_b \approx 0.8$, whereas the measured focal length do not increase as substantially. As noted in the previous chapter, the spherical model is off by a factor of $1/\sqrt{2}$ from the cylindrical model for this scenario, which is the same value by which the predicted focal lengths are larger than those measured in simulations. These results are presented in Fig. 3.5.

To determine the source of the inconsistency between the measured focal lengths and the spherical model, we took one case of an electron at $y_0 = 0.25$ and measured the magnitude of the focusing force as well as the distance travelled in x . The calculated focusing force is consistent with the simulation. However, the transverse distance as measured in the simulation is much closer to the calculated distance using the cylindrical model rather than the spherical model. Specifically, Δx for the spherical model is $\Delta x_{sphere} = 0.85$, while the

measured value is $\Delta x_{sim} = 1.15$, which gives $\Delta x_{sphere}/\Delta x_{sim} = 0.74 \sim 1/\sqrt{2}$. Measured Δx and F_y values are extracted from Fig. 3.6 and reported in Table 3.1.

We hypothesize that the discrepancy in measured and expected Δx values is a result of assumptions we made in our derivation of the analytic focal length formula in Sec. 2.5.1. Specifically, the simulated wakefield may not have suitable qualities for approximating it's shape as a sphere. Eq. 2.5 is a simplified model for the case of $R_b \gg 1$, but in our simulations this condition does not hold. We will thus need to measure the wakefield radius $r_b(\xi)$ and it's derivatives in Fig. 3.1 and test if we are indeed not satisfying Eq. 2.18. If we do not satisfy the conditions needed to approximate the wakefield as a sphere, then there are extra terms not presented in Eq. 2.5 that we may need to take into account. If this hypothesis

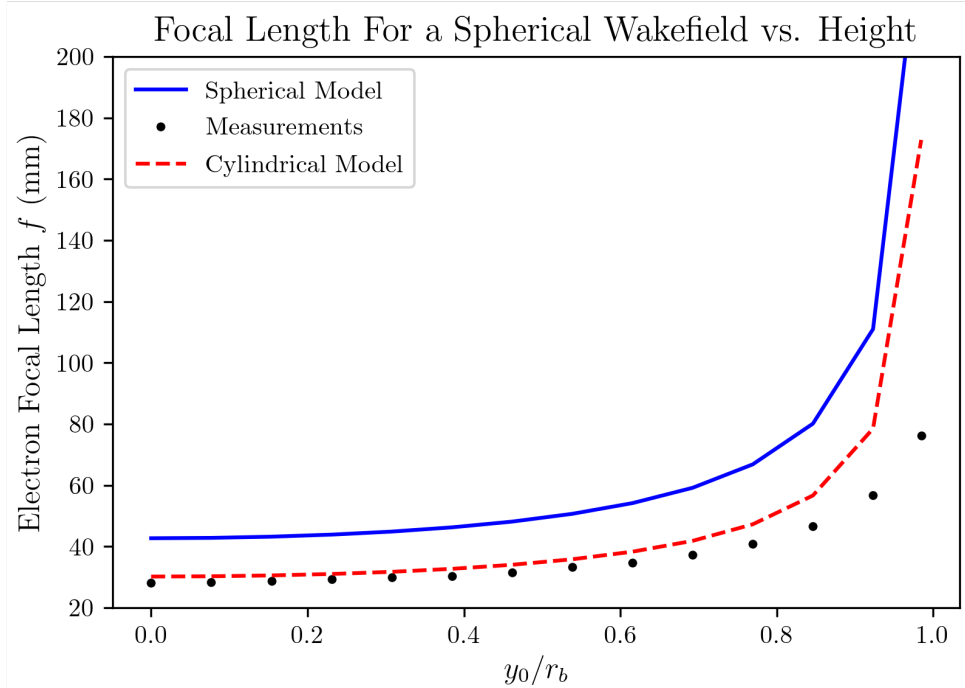


Figure 3.5: Plot showing the focal length of a transverse electron. The horizontal axis is the height of the electron, and the vertical axis is the focal length. The focal length as measured in simulations is shown by the black dots, the expected focal lengths using a cylindrical wakefield model is shown in red, and the expected focal lengths using a spherical wakefield model is shown in blue. Both the theoretical models predict a gradually increasing focal until about $y_0/r_b \approx 0.8$, where both formulas start increasing approximately quadratically. The cylindrical model agrees well with the measured focal lengths until about $y_0/r_b \approx 0.7$, while the spherical wakefield model does not match the data anywhere.

is incorrect, then we will have to examine if additional relativistic effects from the electron beam's momentum, such as length contraction, are a source of error. These hypotheses constitute future work that can be done in order to improve the accuracy of our focusing models.

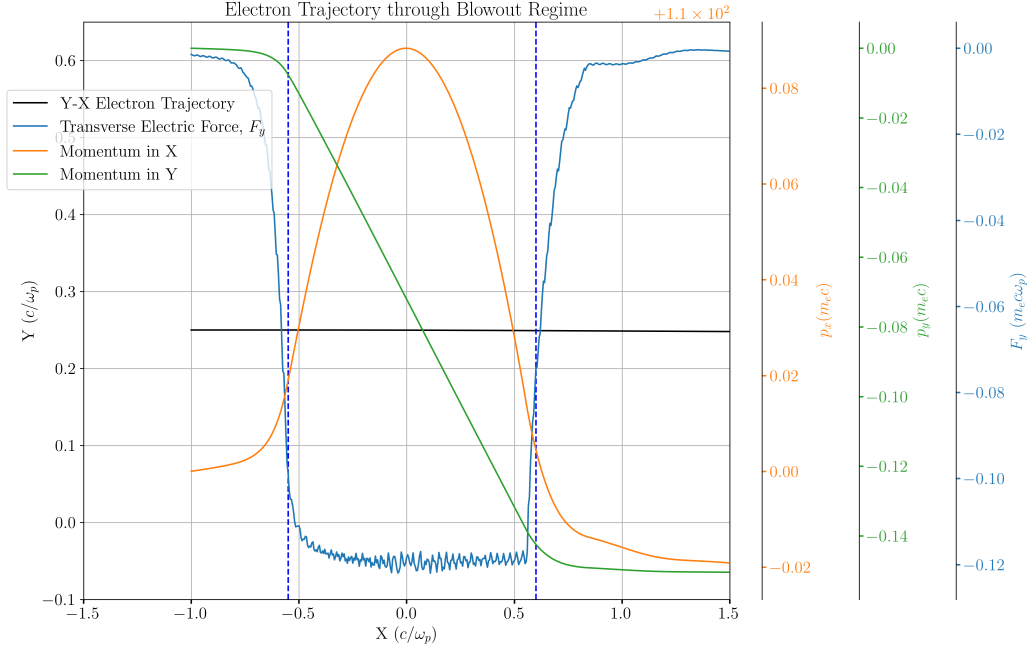


Figure 3.6: Plot of the electron's trajectory in the $x - y$ plane, momenta and focusing force values, while passing through the wakefield. The horizontal axis is the electron's transverse position in x , and the vertical axis is the electron's height. The ballistic trajectory is plotted in black, p_x is plotted in orange, p_y is plotted in green, and F_y is plotted in blue. Note that the tick values for the x-momentum are actually $p_x - 110$. The vertical, blue dashed lines at $x = -0.55$ and $x = 0.6$ show what coordinates were used in the calculation of Δx .

	$\Delta x \ (c/\omega_p)$	$F_y \ (m_e c \omega_p)$
Measured in Simulation	1.15	-0.120
Spherical Model Value	0.85	-0.119
Cylindrical Model Value	1.20	-0.119

Table 3.1: Table showing the expected and measured values for the transverse distance travelled and force for $y_0 = 0.25$. We used $k = 0.475$ to calculate F_y in this table.

Chapter 4

Conclusion

Ultimately, the need for more powerful particle accelerators provides an opportunity for alternative accelerators, such as laser wakefield accelerators, to become the new standard tool with which scientists can probe the structure of matter and the universe. Much of the knowledge of plasma wakefields has been driven by theoretical models and numerical simulations, with experiments also providing proof-of-concept verification of the high accelerating gradients. More experiments need to be done in order to understand crucial properties of these wakefield accelerators, such as beam emittance evolution. With facilities such as the Accelerator Test Facility at Brookhaven National Lab, we are able to perform high quality electron probing experiments to advance our knowledge of the EM field structures inside plasma wakes, from which we can eventually make characterizations of the emittance evolution.

The work presented in this thesis uses a combination of analytic theory and particle tracking simulations to explore how we use electron beams probes as a measurement tool. Using the thin-lens model of laser-driven wakefields, we extended the analytic formula predicting single electron focal lengths to predict where thin bands of electrons reach a minimum width. For thin bands sent at small heights, measuring the distance at which these minimum widths occur show good agreement with our theoretical predictions, and since this minimum

width distance is dependent on the transverse forces the electrons experience, we thus have a diagnostic tool for directly measuring the linearity of the transverse focusing forces. While the low precision of our simulation measurements require us to revisit how the band focusing properties are measured, the first results shown here are promising and still give us a useful experimental diagnostic.

Additionally, our work presents how the masks themselves can be used as a diagnostic in simulation work. Curtain masks allow us to study how high-density structures observed at imaging screens are formed from electrons at various initial radial positions. We showed that a bright outline, which has a similar contour to the outline of the blowout region of the wakefield, is not a result of electrons moving through the wakefield near the edge of the wake, but is instead a result of electrons near the axis all having a similar focal length. This allows us to make qualitative conclusions about the structure of the focusing fields inside the plasma wakes.

Finally, the work done to reformulate our focal length equation for a spherically-modeled wakefield was not successful in improving the accuracy of the focal length predictions. The focal lengths are instead more accurate if we model the wakefield as a cylinder with the maximum wakefield radius, and while the focal length model for the spherical wakefield follows similar trends to the cylindrical wakefield, numerical predictions disagree by a constant factor. We proposed several hypotheses for potential issues that led to this discrepancy, and additional future work is required to determine the source of the discrepancy.

Overall, this research provides a useful analytic framework for electron probing experiments at the ATF. Usage of this diagnostic tool will lead to comparison of theoretical models of the field structures with experimental data, and help to contribute new knowledge of properties of the plasma wakefields.

Bibliography

- [1] Malka, Victor et al. Principles and applications of compact laser–plasma accelerators. *Nature Physics*, 4:447–453, 06 2008.
- [2] Gonsalves, A. J. et al. Petawatt Laser Guiding and Electron Beam Acceleration to 8 GeV in a Laser-Heated Capillary Discharge Waveguide. *Phys. Rev. Lett.*, 122:084801, Feb 2019.
- [3] Zhang, C. J. et al. Capturing relativistic wakefield structures in plasmas using ultrashort high-energy electrons as a probe. *Scientific Reports*, 6, 7 2016.
- [4] Marisa Petrusky. Picturing Plasma: Studying the Simulated Transverse Probing of Laser Wakefield Accelerators. Bachelor’s Thesis, 2021.
- [5] Nicholas Manzella. Development of methods for modeling the interactions of plasma wakefields with a realistic 3D electron probe. Bachelor’s Thesis, 2022.
- [6] Francis F. Chen. *Introduction to Plasma Physics and Controlled Fusion*. Springer International Publishing, 2016.
- [7] W. Lu, C. Huang, M. Zhou, W. B. Mori, and T. Katsouleas. Nonlinear Theory for Relativistic Plasma Wakefields in the Blowout Regime. *Physical Review Letters*, 96(16), 2006.
- [8] Osiris Consortium. OSIRIS, <http://epp.tecnico.ulisboa.pt/osiris>.